Materials Horizons

Accepted Manuscript

This article can be cited before page numbers have been issued, to do this please use: J. Oh, W. Lee, J. Roh, H. Cho and Y. Jung, *Mater. Horiz.*, 2025, DOI: 10.1039/D5MH00942A.

ROYAL SOCIETY OF CHEMISTRY

rsc.li/materials-horizons

View Article Online
DOI: 10.1039/D5MH00942A

New Concepts Statement

This study introduces a novel method for fabricating three-dimensional (3D) structured films via **localized Joule heating** on thermoset elastomers, enabling enhanced sensitivity in soft pressure sensors. Unlike conventional microfabrication techniques that require prefabricated molds and multi-step processing such as photolithography and etching, our approach directly generates 3D surface structures by applying controlled heat to target regions of the elastomer. This mold-free, reconfigurable method enables precise spatial and geometric control of microstructures, thereby simplifying manufacturing while increasing scalability and design freedom.

The resulting localized Joule heating-induced structured films (LHSFs) exhibit significantly improved piezocapacitive sensing performance, including high sensitivity, fast response, and robustness under repeated loading. This work demonstrates a comprehensive application of LHSF-based sensors for subtle pressure detection, robotic gripping, and wearable motion monitoring, as well as the realization of large-area, multi-pixel sensor arrays.

Our findings represent a **conceptual breakthrough** in the design and manufacturing of 3D functional materials for soft electronics. This study not only presents a transformative fabrication approach, but also contributes to the next generation of high-performance, scalable pressure sensors for wearable technologies and interactive systems.

View Article Online
DOI: 10.1039/D5MH00942A

Data Availability Statement

All data supporting the findings of this study are included in the main article and its Supplementary Information files.

View Article Online
DOI: 10.1039/D5MH00942A

ARTICLE

Three-Dimensional Morphology in Localized Joule Heating-Induced Structured Films for Enhanced Sensitivity in Soft Pressure Sensors

Received 00th January 20xx,
Accepted 00th January 20xx

DOI: 10.1039/x0xx00000x

Jiyoon Oh [a,b †], Wookjin Lee [c], Jeongkyun Roh [b], Hanchul Cho [a, *], and Young Jung [d, e, *]

Manufacturing the well-designed three-dimensional (3D) structures of a soft elastomer's surface is essential for achieving a highly sensitive soft pressure sensor and for pursing advanced applications. While soft pressure sensors with 3D structures have previously been developed through methods such as prefabricated micro-pattern molds and elastomer replication, challenges such as limited geometric flexibility and the necessity for multi-step fabrication processes remain. This study demonstrates a novel approach for fabricating 3D structures by employing localized joule heating on thermoset elastomers, aimed at enhancing the sensitivity of the soft pressure sensors. The thermal fields generated by localized joule heating apply heat only to a designed area of the thermoset elastomer, enabling the formation of 3D structures in specific shapes. The localized joule heating-induced 3D-structured film (LHSF) is utilized in a piezocapacitive soft pressure sensor. The sensor exhibits a high sensitivity of 1.352 kPa-1 in the low-pressure range with a fast response time (0.59 s), excellent repeatability, and long-term stability. Finally, the advanced applicability of the proposed soft pressure sensors in diverse plans including grip pressure detection, motion monitoring, and multi-pixel pressure array pad is demonstrated.

Introduction

Recently, soft pressure sensors have attracted significant attention due to their flexibility, versatility, and applicability [1]. These sensors can be utilized for advanced and potential applications such as in wearable devices [2-4], health monitoring [5-7], soft robotics [4, 8, 9], and human-machine interfaces [8, 10, 11]. These tasks typically involve the interaction between the human user and the device, ranging from soft touch (0-10 kPa, low-pressure range) to the handling of objects (10-100 kPa, medium-pressure range). For many of these potential soft-touch applications, soft pressure sensor with a high level of sensitivity is required for the delicate sensing of pressure that matches the sensing capability of the human skin. Soft pressure sensors are classified according to their sensing mechanism, which includes piezoresistive [12-14], piezocapacitive [2, 15-18], piezoelectric [2, 19], or piezo transmittance [20-22] types, among others. Piezocapacitive sensors are soft pressure sensors that convert applied pressure into a capacitance signal. They are widely used because of their simple structure, high stability, high repeatability, and low hysteresis.

Recently, to enhance the sensing performance of a piezocapacitive pressure sensor, many researchers have utilized soft, compressible, and deformable elastomer [2]. However, due to the intrinsic material properties of the soft and compressible elastomers (e.g., viscoelasticity), the sensing performance of elastomer-based pressure sensors is still limited by low sensitivity, and long response time, and significant hysteresis [22]. An efficient strategy for fabricating soft pressure sensors with excellent sensing performance is the use of three-dimensional (3D) structured films, such as pyramids [16, 23], domes [24-26], and others [27]. These 3D structures generate a large deformation when pressure is applied, which significantly enhances sensing performance including sensitivity and allows even small pressures to be clearly detected. In addition, the use of 3D-structured films as the dielectric layer can minimize the viscoelastic property of the soft elastomer, resulting in fast response time, excellent repeatability, and reduced hysteresis.

Various methods have been proposed for producing 3D structures of different geometries, including 3D printing [2, 28-30], prefabricated micro-pattern mold [24, 31], and pre-strain techniques [32]. These approaches offer a significant advantage in terms of compatibility with a wide range of elastomers that vary in both Young's modulus and biocompatibility. For example, Tee et al. developed a piezocapacitive flexible pressure sensor based on 3D structured elastomers generated by the photolithography and silicon etching process [16]. They demonstrated that sensitivity can be tuned by using optimization of the structural geometries (i.e., sidewall angled structures) and density control (i.e., spacing of the structures).

[a.] Extreme Process Control Group, Korea Institute of Industrial Technology (KITECH), Busan 46938, Republic of Korea
[b.] Department of Electrical and Electronic Engineering, Pusan National University, 2, Busandaehak-ro 63beon-gil, Geumjeong-gu, Busan 46241, Republic of Korea
[c.] School of Materials Science and Engineering, Pusan National University, 2, Busandaehak-ro 63beon-gil, Geumjeong-gu, Busan 46241, Republic of Korea
[d.] Major of Mechanical Engineering, Pukyong National University, 45 Yongso-ro, Nam-gu, Busan 48513, Republic of Korea
[e.] Department of Intelligent Robot Engineering, Pukyong National University, 45 Yongso-ro, Nam-gu, Busan 48513, Republic of Korea

‡ Supplementary Information available: details of any supplementary information available should be included here. See DOI: 10.1039/x0xx00000x
*These authors contributed equally

View Article Online
DOI: 10.1039/D5MH00424A

Baek et al. suggested capacitive-type flexible pressure sensor based on wrinkled structures by stretching and releasing with ultraviolet-ozone (UVO) exposure [27]. Because UVO treatment form a stiff silicate layer on the soft elastomer surface, wrinkled structures are generated on the surface for mismatch between the elastic modulus of the soft elastomer layer and silicate layer [27]. While these approaches could be used to produce soft pressure sensors with high sensing performance, it is still challenging in terms of limited geometry flexibility and multi-step manufacturing. The proposed methods require additional process such as patterned-mold fabrication and UVO treatment for formation of stiffness layer, which have limitations in terms of fabrication flexibility. Therefore, a novel approach is required to present sensitive soft pressure sensors by ⅰ) manufacturing 3D structures with high geometry flexibility without the use of conventional processes and ⅱ) advancing the fabrication methodology.

In this work, to address these issues, we propose a novel strategy for fabricating 3D-structured films for soft pressure sensors utilizing localized joule heating processes on thermoset elastomers. The 3D structure was fabricated using a thermoset elastomer and the localized joule heating process, which generates thermal fields to a designed area. Notably, our proposed method not only allows the fabrication of reproducible and scalable 3D structures on the surface without conventional fabrication processes (i.e., mold fabrication, metal-deposition, and etching), but also enables the fabrication of 3D structures by controlling parameters. Finite-element method (FEM) simulations were employed to analyze the distribution of thermal fields by joule heating across various conditions, including time and profile. We applied the localized joule heating-induced 3D-structured films (LHSF) to soft pressure sensors and evaluated the sensing characteristics under static (i.e., sensitivity and stability) and dynamic (i.e., repeatability, response time, and long-term stability) loading. Finally, the soft pressure sensors based on LHSF were successfully applied in advanced applications including grip pressure detection, motion monitoring, and multi-pixel pressure array pad.

Results and Discussion

Fabrication Process for Localized Joule Heating-Induced 3D-structured films

Figure 1 illustrates the proposed fabrication methods for localized joule heating-induced 3D-structured films (LHSF). Firstly, we prepared a bare polyimide (PI) film with a thickness of 50 μm (Figure 1a and Figure S1a). The laser-induced graphene (LIG) was grown directly on a PI film using CO2 laser treatment with specific scanning power and interval between the scan steps, and then sensing lines were connected to both electrode pads using silver epoxy (Figure 1b and Figure S1b). The LIG technique can make the scalable, cost-effective, rapid, delicate micro-patterning of conductive graphene by the photothermal effect between a CO_2 laser treatment and PI film [33]. To optimize conductivity while controlling joule heating, the electrode pads at both ends of the LIG were designed with a width of 10 mm, whereas the central LIG region was patterned with a minimum width of 200 μm to maximize localized heating effects. Then, a well-mixed liquid polydimethylsiloxane (PDMS) precursor was uniformly coated onto the patterned LIG and PI film using a doctor blade film coater, forming a 1.5 mm-thick PDMS layer

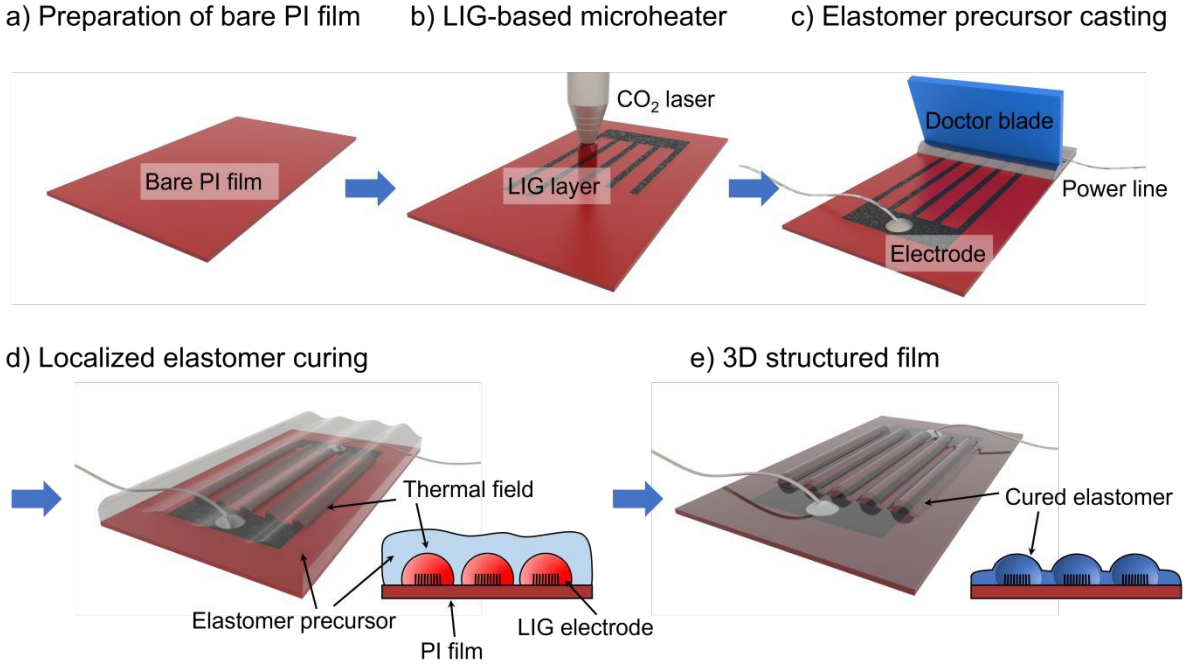

Figure. 1 Fabrication method of the patterned elastomer using localized joule heating-induced 3D-structured films (LHSF). a) Preparation of bare polyimide (PI) film. b) Fabrication of microheater for joule heating based on laser-induced graphene (LIG). The highly conductive LIG-based microheater was manufactured through a simple CO2 laser treatment. c) Liquid elastomer precursor casting on the substrate using doctor blade film coater. d) Localized joule heating for elastomer curing. The elastomer is cured based on the thermal field generated by the LIG-based microheater, allowing precise control of the curing area. e) Fabricated 3D structures along with the LIG-based microheater.

View Article Online
DOI: 10.1039/D5MH00948A

(Figure 1c). Localized joule heating, also known as ohmic heating, converts electrical energy into thermal energy, selectively curing the PDMS in designated regions. This technique enables high reproducibility, scalability, and cost-effective fabrication, making i t a valuable method for industrial applications (Figure 1d). Once heating was applied, only the exposed regions with LIG underwent thermal curing, while the unheated PDMS remained in its liquid state. Finally, when the remaining liquid PDMS was then removed by washing with a PDMS diluent, resulting in the formation of precisely patterned 3D structures aligned with the LIG-based microheater (Figure 1e and Figure S1c). In this work, additional comparisons with previously reported approaches were conducted in terms of structural precision, material applicability, capability for fabricating complex architectures, and other relevant factors (Table S1, Supporting Information). These comparisons demonstrate that this approach can significantly simplify the fabrication process, reduce the overall cost, and enhance the scalability, making it well-suited for the development of flexible and pressure-sensitive electronic devices.

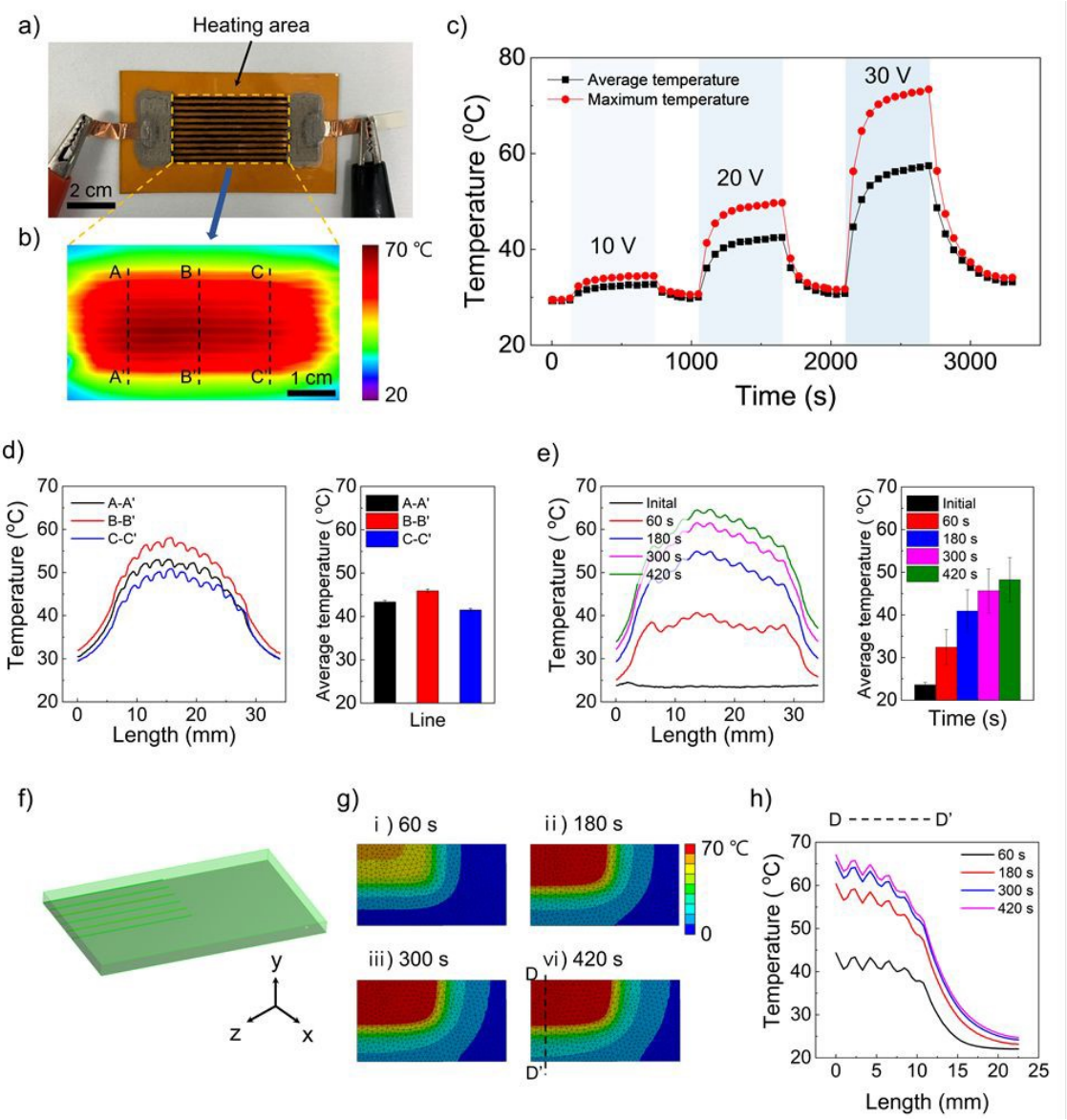

Figure. 2 Verification of localized joule heating characteristics of the LIG-based microheater. a) Fabricated LIG-based electrode for the localized joule heating. b) Real-time measurement of the temperature distribution using thermal imaging camera. c) Stepwise localized heating characteristics of the LIG-based microheater at different applied voltages. d and e) Cross-sectional temperature profile according to the profile and time. f) Representative volume element (RVE) model based on the LIG-based microheater. g) The generated thermal field according to time. h) Numerical simulation results of temperature distribution according to time.

Optimization of Joule Heating Conditions for Fabrication of 3D-structured films

To verify the feasibility of fabricating LHSF using our proposed method, we measured the thermal characteristics induced by joule heating in an LIG-based microheater (Figure 2). Figure 2a illustrates the experimental setup with microheater and power supply. Eleven LIG-based microheater lines were directly fabricated on a cleaned PI film using CO_2 laser treatment, and sensing lines were connected to the electrode pads using silver epoxy. Figure S2 shows field emission scanning electron microscopy (FE-SEM) images of the LIG-based microheater and

electrode pad on a PI film. The widths of each LIG-based microheater line were uniformly set to 200 μm, which is the minimum feature size achievable with our CO_2 laser equipment. The spacing between adjacent LIG-based microheaters was approximately 300 μm to prevent overlapping of the thermal fields generated by neighboring heaters. Notably, the electrode pad exhibited a highly dense LIG growth due to the higher CO_2 laser power, whereas the microheater region showed relatively lower-density LIG formation. We also measured the surface profile of the fabricated LIG-based microheater under varying fabrication conditions (Figure S3, Supporting Information). In addition, the average resistance and standard deviation of the LIG-based microheater was measured 1.1011 ± 0.013 kΩ (Figure S4, Supporting Information). These results indicate that the proposed CO_2 laser treatment method enables the fabrication of reproducible LIG-based electrodes and microheaters. Figure 2b presents the infrared (IR) image of LIG-based microheater under an applied electrical bias of 30 V, demonstrating localized joule heating characteristics. The maximum temperature reached approximately 70 ℃, and thermal profile was clearly observed due to joule heating. For a single LIG-based microheater line, the temperature was insufficient to cure the elastomer (Figure S5, Supporting Information). Conversely, when using 22 LIG-based microheater lines, the thermal fields overlapped, resulting in an indistinct thermal profile. The procedures for adjusting and optimizing the 3D structure are summarized in Figure S6 and S7 of the Supporting Information. This reduces thermal confinement and causes the microheaters to overlap. When the spacing between electrodes is too narrow, the 3D structures merge due to the overlapping thermal field caused by joule heating (Figure S6 in Supporting Information). 3D structures were fabricated using elastomer layers of varying thicknesses. A 1.5 mm-thick layer produced well-defined 3D features with a height of ~150 μm (Figure S7, Supporting Information), which was subsequently applied to the pressure sensor. We also analyzed the cross-sectional temperature profiles along specific lines (BB’ evaluating average/maximum values and thermal recovery properties at different electrical biases. At 10 V, the average temperature was 31.93 ℃, and the maximum temperature was recorded as 33.53 ℃, resulting in a small temperature difference of 1.60 ℃ (Figure 2c). At 30 V, the temperature increased significantly, with the average and maximum temperatures measured at 52.15 and 65.97 ℃, respectively. Notably, the temperature increased rapidly with the applied voltage. The thermal distribution due to joule heating in the LIG-based microheater was recorded using an IR camera. Figure 2d shows the cross-sectional temperature profiles at 30 V along the specific lines (AA’, BB’, and CC’ in Figure 2b). Among these three regions, the highest temperature profile was observed at the center (BB’). The average temperature at the first and last positions was 43.32 ± 0.42 ℃ and 41.45 ± 0.36 ℃, respectively, whereas the middle region exhibited a higher average temperature of 45.88 ± 0.41 ℃, which is ≈1.10 times higher than the outer regions. Additionally, we also checked that the detailed temperature profiles along specific liens (BB’) under various time (Figure 2e). In case of 60 and 180 s, the temperature profile dramatically increased than that of initial state. After that, average temperature profiles were almost saturated, two profiles of 300 and 420 s showed high temperature as about 70 °C. The average temperature of the specific line (BB') at each time point was measured as 23.61 ± 0.57 °C, 32.43 ± 4.13 °C, 40.87 ± 5.00 °C, 45.63 ± 5.17 °C, and 48.25 ± 5.19 °C, respectively.

Numerical simulation was conducted using a representative volume element (RVE) to understand the joule heating characteristics of the LIG-based microheater according to the profile and time. Figure 2f depicts the 3D model, including LIG-based microheater and PI film for numerical simulation of thermal field. As shown in Figure 2g, the thermal field rapidly generated according to the time, and the sufficient thermal field for localized elastomer curing (i.e., 70 °C) was reached at 180 s. Figure 2h shows the cross-sectional temperature profiles along specific lines (DD’) under various time. In 60 s, maximum temperature was calculated as 32.42 °C. As the time increases, average temperature was clearly saturated, two curves of 300 and 420 s almost overlapped. In addition, thermal field by LIG-based microheaters was clearly observed. The simulation results were similar with those obtained measured results. These results indicate that the LIG-based microheater generates a sufficient thermal field to cure the commercial thermoset elastomer (e.g., PDMS, EcoflexTM, and Dragon SkinTM Series), even in the form of 3D shapes.

Observation of Localized Joule Heating-Induced 3D-structured films

As mentioned above, the proposed localized joule heating method enables the manufacturing of reproducible and scalable 3D structures along with the LIG-based microheater. Figure 3 shows the characterization results of the 3D-structured films based on the LIG-based microheater and localized joule heating process for 16 minutes. Figure 3a shows photographs of the fabricated LHSF. The cured elastomer was fully embedded in the LIG, and as a result, the LHSF exhibited high mechanical robustness under bending deformation. The profiles of the LHSF were measured using a 3D confocal scanning microscope to observe the 3D structures. The 3D structures with a maximum height of up to 150 μm were clearly observed (Figure 3b). The 3D structures were formed along with the LIG-based microheater with high uniformity. Figure 3c shows the cross-sectional profiles along specific lines (AA’). To compare the surface profile of 3D structure by joule heating, we prepared additional sample (noted as “uniform heating two-dimensional structured films, UHSF), which was cured at oven at 70 °C (Figure S8, Supporting Information). In the case of UHSF, a flat surface is formed regardless of the presence of underlying LIG electrodes (Figure S9b). As shown in Figure S10 and 11, this is because the uniform heat distribution occurs throughout the elastomer precursor, leading to homogeneous curing throughout the materials. The uniform heat distribution resulted in the flat surface across the elastomer surface, as confirmed by thermal and morphological analyses (Figure S12). The UHSF exhibited smooth surface and a maximum height of only 4 μm. To compare the morphology according to manufacturing methods such as localized joule heating and

View Article Online
DOI: 10.1039/D5MH00943A

oven heating, three roughness parameters (arithmetical mean height (Ra), root mean square deviation (Rq), and maximum height of profile (Rz)) were measured using confocal laser microscope (Figure S13, Supporting Information). The average Ra significantly increased from 1.12 to 34.54 µm. The Rq and Rz also increased from 1.45 and 7.14 to 39.98 and 135.49 µm. This significant difference in height means that the superior roughness. Therefore, we selected a joule heating time of 16 min utes for further surface characterization and sensor evaluation.

Sensing Performance of the Soft Pressure Sensor

Figure 4a shows a sensor structure of the sensitive, soft pressure sensor, where the LHSF is used as a dielectric layer for pressure sensing and a LIG-based microheater on a PI substrate for joule heating acts as a bottom electrode. Furthermore, the metal-deposited PI substrate is placed face-to-face with a LHSF as the top electrode. The detailed working principle of the soft pressure sensor is shown in Figure 4b. The 3D structure enables stress concentration, reducing stiffness of the dielectric layer. Because of the reduced stiffness, the dielectric layer based on 3D structures offers a large deformation at the same pressure, resulting in high sensitivity. Furthermore, the high dielectric constant of the elastomer, utilized in the fabrication of the 3D structures, increased the percolation effect; therefore, the sensitivity of the soft pressure sensor was dramatically enhanced than that of the soft pressure sensor based on flat surface under identical applied pressure. By utilizing accessible and universally applicable LIG-based microheater electrodes, we successfully fabricated 3D structures not only on a single surface but also on both sides of the substrate (Figure S15). This result indicates the potential of the joule heating process for constructing complex and diverse 3D geometries.

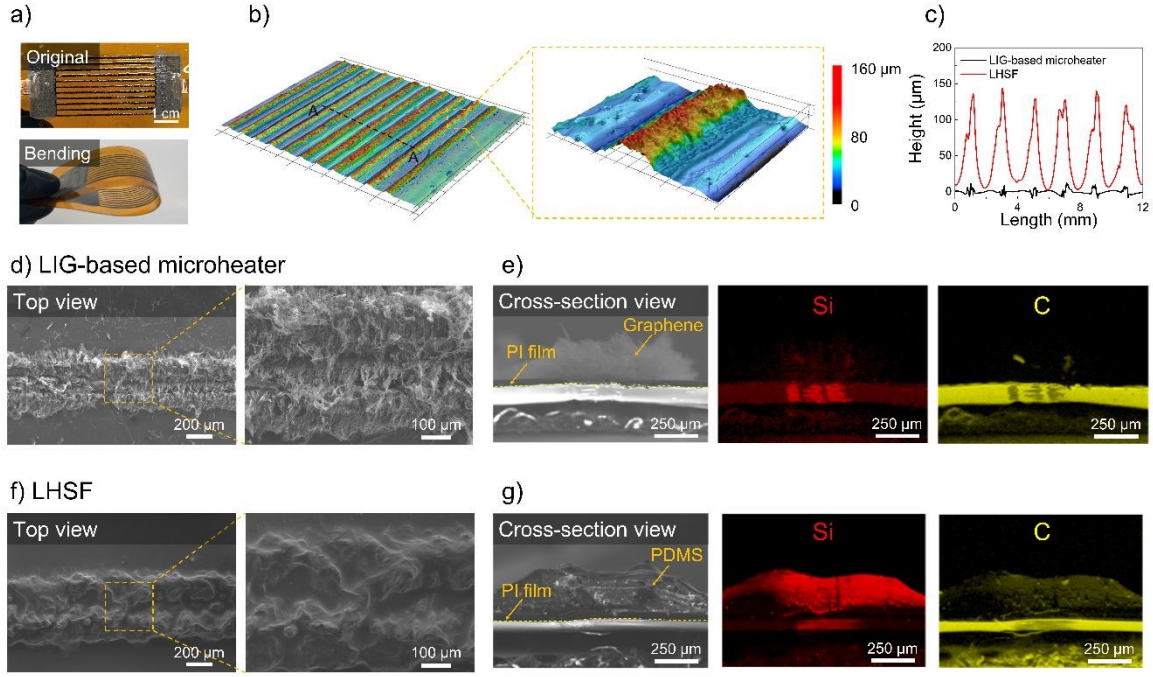

Figure. 3 Characterization of the fabricated 3D-structured films based on LIG-based microheater and localized joule heating process. a) Photographs of the original and bent states of the 3D-structured film demonstrating its flexibility. b) Surface profile measurements of the 3D-structured film. C) Cross-sectional profiles along specific lines to verify the 3D structures. The height of the LIG-based microheater is approximately 3~7 µm, while the height of the 3D-structured film (LHSF) reaches up to 150 µm, indicating the successful fabrication of 3D structures on the surface. d-g) Field-emission scanning microscope (FE-SEM) images and energy-dispersive X-ray spectroscopy (EDS) characterization of the LIG-based microheater and 3D structures. d) The top view shows the entangled and dense distribution of LIG, and the cross-section view shows the layered structure with the LIG layer on the PI film. e) EDS mapping of silicon (Si) and carbon (C) distribution in the cross-section of the LIG on PI film. f) The 3D structure was fabricated along with LIG-based microheater. g) EDS mapping of Si and C distribution in the cross-section of 3D-structured films. The Si and C peaks were significantly increased for the cured PDMS.

capability of the localized joule heating method in creating 3D structures compared to uniform heating, which is limited in its ability to induce significant 3D structuring.

Figure 3d-g shows field emission scanning electron microscopy (FE-SEM) images and energy-dispersive X-ray spectroscopy (EDS) characterization of the LIG-based microheater and 3D structures, respectively. The fabricated LIG-based microheater exhibited entangled and dense distribution. In addition, when we analyzed the EDS mapping results, only a few peaks of silicon (Si) and carbon (C) peaks were observed. When the elastomer was cured by localized joule heating, well-designed 3D structure was clearly observed (Figure 3f). When we checked the EDS mapping results of the LHSF, a patterned 3D structure was formed on the surface and Si and C peaks were significantly increased for the cured PDMS. These results indicate that the proposed localized joule heating method effectively cures the elastomer and forms well-designed 3D structures. We also fabricated 3D-structured films using localized joule heating with curing times ranging from 4 to 24 minutes (Figure S14). At curing times shorter than 16 minutes, the PDMS did not cure sufficiently. Conversely, at longer curing times, an excessive amount of PDMS cured, leading to a reduction in surface

View Article Online
DOI: 10.1039/D5MH00942A

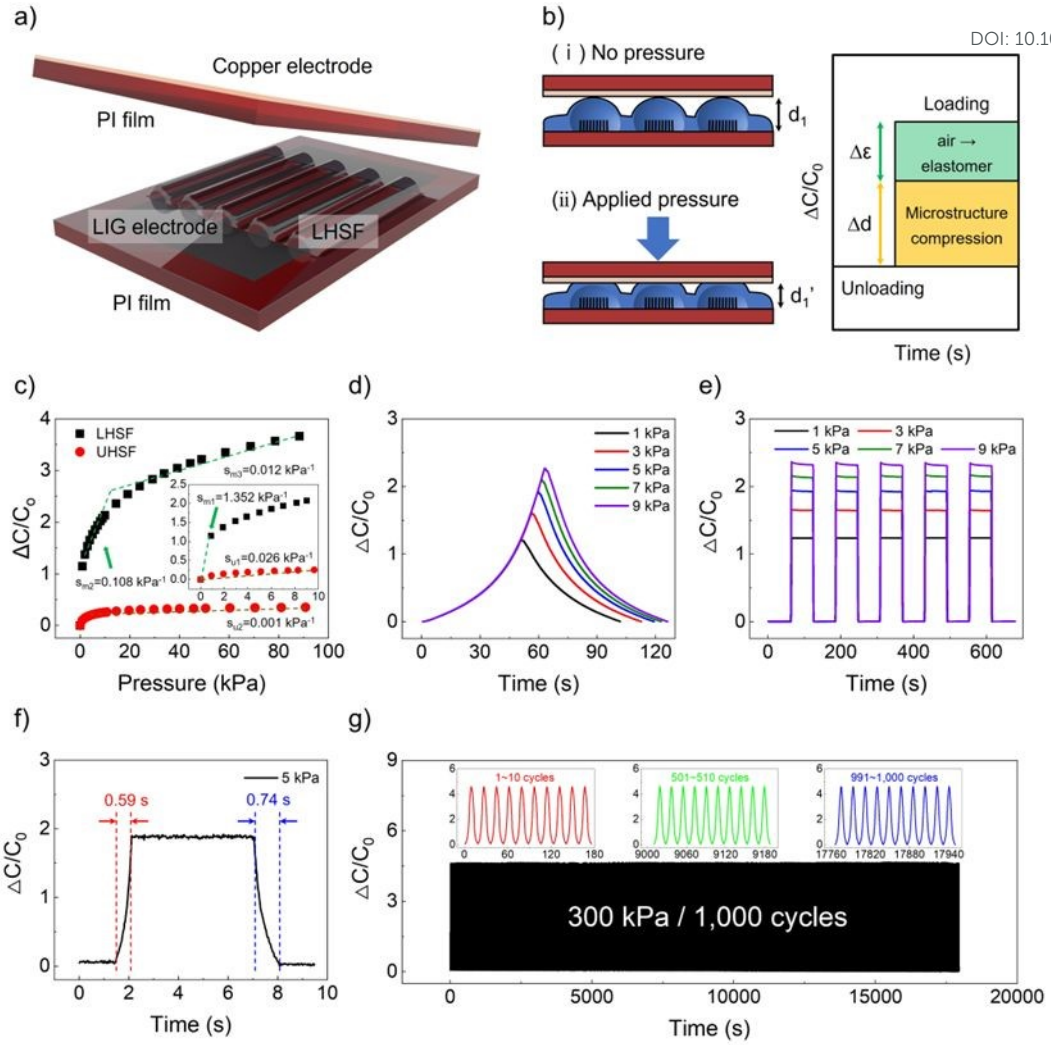

Figure. 4 Sensor structure and sensing performance of the soft pressure sensor based on LHSF. a) Schematic illustration of the LHSF-based soft pressure sensor. b) Sensing mechanism of the fabricated soft pressure sensor. c) Measured sensitivity of the soft pressure sensor under the pressure range of 0–100 kPa. The sensitivity of the LHSF-based sensor was ~52 times higher than that of the sensor with a UHSF. d) Stability tests over different duration under various applied pressures. e) Repeatability tests (0–120 s) under various applied pressures. f) Response time of the LHSF-based soft pressure sensor under loading at 5 kPa. The 10% to 90% rising time (tr) and 90% to 10% falling time (td) are measured approximately 0.59 s and 0.74 s, respectively. g) Results of the reliability tests at 300 kPa over 1,000 cycles. The red, green, and blue graphs in the inset show the results of the first, middle and last 10 cycles, respectively.

Figure 4c depicts the sensitivity of the soft pressure sensor based on LHSF and UHSF in the pressure range of 0–100 kPa. The sensitivity is defined as $S = \delta(\Delta C/C_0)/\delta p$, where C and C_0 denote the capacitance with and without applied pressure, respectively, and p denotes the applied pressure. The soft pressure sensor based on the LHSF exhibited three different linear sensitivities under applied pressure. In the first linear section up to 1 kPa, the pressure response exhibited a linear behavior and high sensitivity of 1.352 kPa^{-1}. Notably, the sensitivity of the proposed soft sensor is ~52 times higher than that of the sensor with a UHSF. The second linear section exhibited a sensitivity of 0.108 kPa-1 at 1–10 kPa, which is ~108 times higher than that of the sensor with a UHSF. In the third linear section 10–100 kPa, which exhibits the lowest sensitivity of 0.001 kPa^{-1}, the 3D structures are fully compressed, acting as a bulk elastomer, and the sensitivities of the two sensors are very similar. We compared the sensing performance of the proposed sensor, key metrics—such as sensitivity and pressure range—were benchmarked against those of previously reported strategies. As shown in Figure S16, 3D microstructured film-based sensors exhibit higher sensitivity in the low-pressure range, but have a limited pressure range (saturating near 10 kPa), which makes them generally optimized for ultra-low-pressure detection (e.g., ~1 kPa). In contrast, our study suggests that LHSF-based sensors can maintain high sensitivity over a wide pressure detection range up to 100 kPa. The sensor proposed in this study, which is based on a LHSF, maintains high sensitivity over a wide pressure range of up to 100 kPa—without the need for expensive equipment or complex fabrication processes typically associated with conventional semiconductor manufacturing. Owing to its high-aspect-ratio and uniformly distributed 3D-patterned architecture, the sensor can detect subtle stimuli under low-pressure conditions and simultaneously withstanding high-pressure environments.

View Article Online
DOI: 10.1039/D5MH00942A

Figure 4d shows the measured relative changes of capacitance in the LHSF-based soft pressure sensor with loading and unloading on time in 10% strain min^{-1}. The soft pressure sensors show a stable signal at various pressures (1, 3, 5, 7, 9 kPa). To evaluate the reproducibility of the sensors, various pressures (1, 3, 5, 7, 9 kPa) were applied to the sensor and relative change in capacitance is measured (Figure 4e). No deviation of the capacitance occurred with and without pressure. We also verified the response time of the soft pressure sensors measured in 5 kPa (Figure 4f). The 10% to 90% rise time (t_r)and 90% to 10% fall time (t_d) were measured to be 0.59 s and 0.74 s respectively. The LHSF-based soft pressure sensors consist of a PDMS support structure with excellent elastic properties. Even when pressure is immediately applied and removed, the 3D structure returns quickly to its original shape without any permanent deformation. For the fabricated sensors to be used in practical applications, they must maintain stable sensing characteristics under repeated pressure loading. The LHSF enabled the sensor to achieve comparable sensitivity in the low-pressure range and, notably, to maintain this sensitivity even under high-pressure conditions—surpassing many existing approaches. Unlike conventional sensors, which often show high sensitivity only within a narrow sensing range, the proposed sensor demonstrates uniform sensitivity across a broad pressure range. We evaluated the reliability and long-term stability of our sensor by applying 1,000 repeated compression/release cycles under a pressure of 300 kPa (Figure 4g). Neither a shift in the sensing response nor a structural change in the sensor was observed during 1,000 cycles of compression. The inset values in the middle of the graph show the average responses and standard deviations for each cycle. In the initial 1–10 cycles, the average response was 4.603, and the standard deviation was 1.687%. Similar values were consistently measured throughout repe ated compression

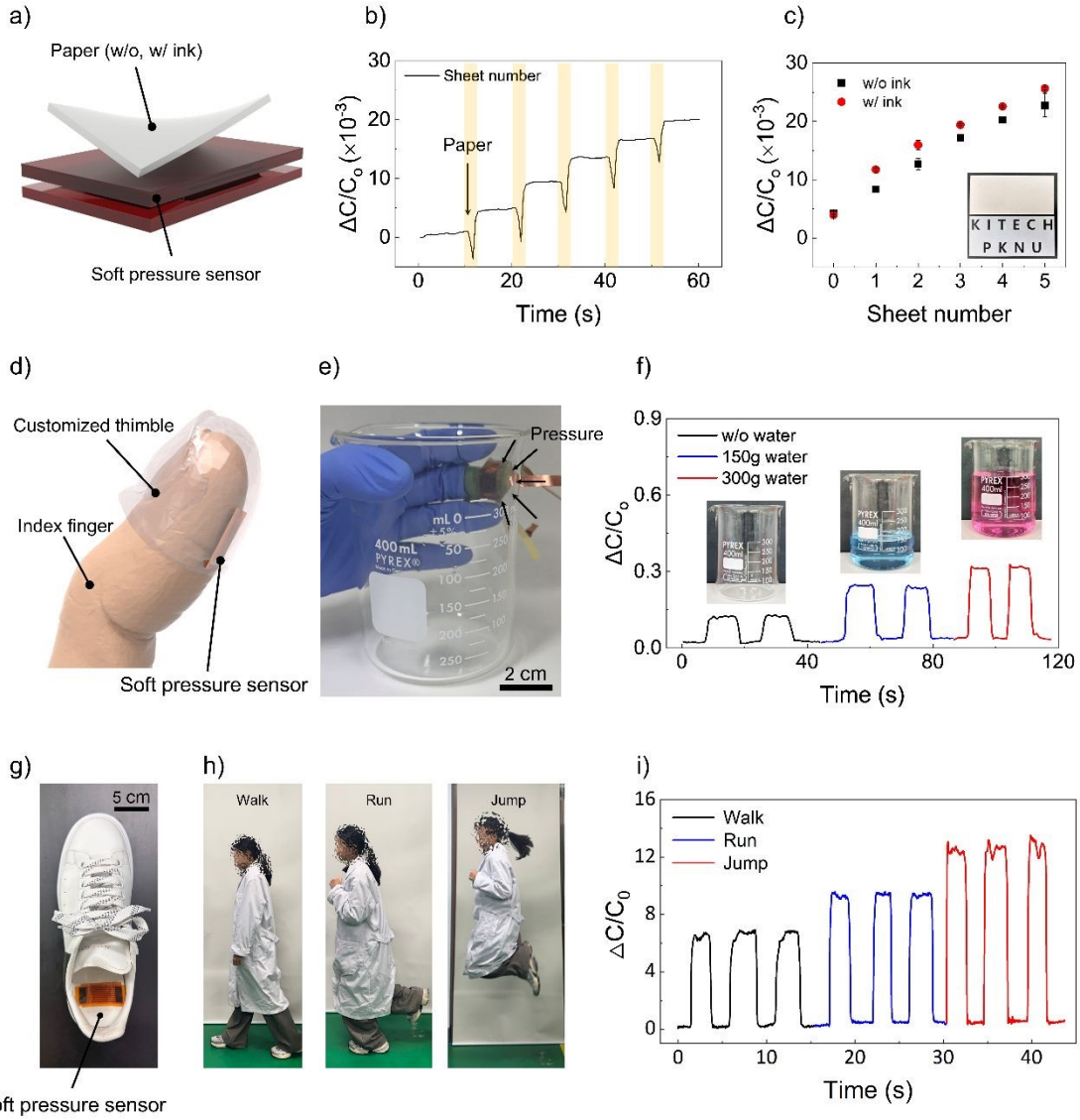

Figure. 5 Demonstration of the soft pressure sensor applications based on the proposed LHSF for different pressure ranges. a) Schematic illustration of the detection subtle pressure variations. b) Sensor signal when ultra-lightweight paper was sequentially placed on the soft pressure sensor. c) Detection of pressure between plain paper and paper with ink. d-e) Schematic illustration and photographs of demonstration of the object recognition on middle finger. f) Sensor signal on the middle finger. The responses clearly recognized the different water loads. A colorant has been added to clarify the water level. g) The soft pressure sensor on the shoe insole. h) Images of three different activities. i) Sensor signal with different motion such as walking, running, and jumping.

View Article Online
DOI: 10.1039/D5MH00913A

cycles. For example, in cycles 501-510, the response and standard deviation were 4.625 and 2.001%, respectively. In cycles 991-1000, the response and standard deviation were 4.610 and 1.333%. In addition, the roughness parameters of the LHSF before and after the reliability test show that there was no significant change occurred in the structure of their high elasticity and mechanical stability (Figure S17, Supporting Information). The proposed sensor, based on the 3D structures, demonstrated excellent sensing performance in terms of sensitivity, sensing range, response time, and reliability than previously developed sensors.

Soft pressure sensor applications

Given the excellent sensing characteristics such as high sensitivity, wide pressure range, stability and reliability under static and dynamic applied loading, the proposed soft pressure sensors based on LHSF are applicable to various potential applications. As one of the practical applications, we explored their capability in detecting subtle pressure variations (Figure 5a). Ultra-lightweight paper was sequentially placed on the soft pressure sensor based on the LHSF, and the sensor successfully detected the subtle pressure changes (Figure 5b). Furthermore, it distinguished differences in capacitance between plain (16.4 mg, 0.7145 Pa) and paper with ink (18.1 mg, 0.7892 Pa), as shown in Figure 5c. Even when the number of plain paper was increased to five, the maximum standard deviation in capacitance change remained below 2, indicating excellent reproducibility of the measurements. The proposed soft pressure sensor showed high flexibility and high sensitivity in low-pressure range. Based on this superior sensitivity, our soft pressure sensor was applied to electronic skin for object recognition. This application allowed for the detection of pressure variations when handling objects of different weights. A custom-fitted thimble embedded with the fingertip-shaped soft pressure sensor (Figure 5d) was fabricated to seamlessly conform to the user's finger. Using this sensor-integrated thimble, we demonstrated that the electronic skin successfully detected a beaker with varying water weights (0, 150 g, and 300 g) (Figure 5e). As shown in Figure 5f, the fingertip-shaped soft pressure sensor successfully recognized the different water loads, demonstrating its practicality in such applications. The soft pressure sensor showed high reliability under both static and dynamic loading conditions across a wide pressure range. Based on these advantages, the proposed sensor was integrated into a shoe insole–an application that demands not only stability but also exceptional sensitivity. This integration allowed for the monitoring of different motions. Figure 5g presents photos of the shoe insole with the attached sensor, while Figure 5h and 5i show photos and capacitance measurements corresponding to different activities, including walking, running, and jumping, recorded sequentially. The sensor exhibited distinct relative capacitance values for each

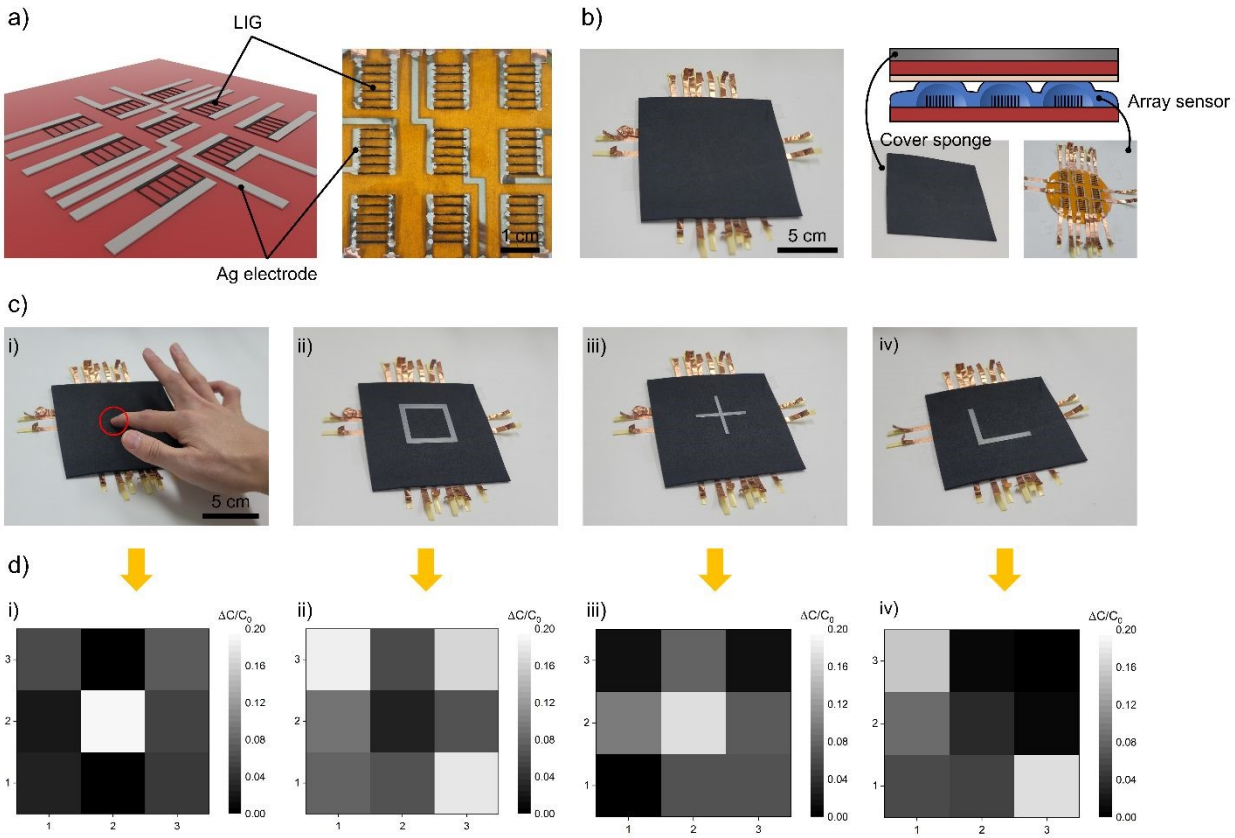

Figure. 6 Demonstration of the multi-pixel pressure array pad based on the soft pressure sensor for pattern recognition. a) Schematic representation of the LIG-based microheater and Ag electrode. b) Images of the fabricated multi-pixel pressure array pad, which is composed of a cover sponge, top electrode, and LHSF layer. c) Visualization of different applied pressure patterns, including a middle finger touch, square, cross, and L-shape, interacting with the multi-pixel pressure array pad. d) Pattern recognition results, where brighter pixels indicate greater capacitance changes. The variations in capacitance across individual pixels enable clear distinction of the applied patterns.

View Article Online
DOI: 10.1039/D5MH00843A

motion type, further validating its capability to accurately detect and distinguish pressures of varying ranges. These findings confirm that the proposed soft pressure sensor is highly effective in both static and dynamic environments, offering robust and sensitive performance for a wide range of applications, including electronic skin and wearable devices.

As mentioned above, the proposed methods for forming a 3D structure using an LIG-based microheater and localized joule heating offer significant advantages, including easy of fabrication, high reproducibility, scalability, and cost-effective process. This approach enables the creation of customizable 3D-structured films in various patterns and shapes. Based on these advantages, we demonstrated the potential of this technology through the development of a multi-pixel pressure array pad with 3 × 3 pixels (Figure 6). Figure 6a illustrates a schematic and corresponding images of the array LHSF layer, which serves as the bottom electrode of the pad. The arrayed LIG layer was fabricated using a CO_2 laser scanning for microheater formation, followed by metal deposition for the sensing electrode. The fabricated multi-pixel pressure array pad is composed of a cover sponge for user comfort, a top electrode, and the LHSF layer (Figure 6b). The pad measures 12 × 12 cm^2, and when pressure is applied, it detects variation by measuring capacitance changes at each pixel. As illustrated in Figures 6c and 6d, pattern recognition results show distinct capacitance variations, with brighter pixels indicating greater pressure-induced variations. When a light press was applied, the central pixels exhibited a noticeably higher response than the surrounding areas. Furthermore, placing acrylic patterns of different shapes (square, cross, and L-shape) on the pad resulted in clear and distinguishable capacitance variations at corresponding pixels (Figure 6d). These results indicate that the proposed LIG-based microheater and localized joule heating method enables the efficient fabrication of highly sensitive and customizable multi-pixel pressure array pads. This scalable and cost-effective approach holds significant potential for diverse applications, including tactile sensing, wearable electronics, and human-computer interaction. Its demonstrated ability to discern complex pressure patterns makes it highly suitable for advanced pattern recognition and precise pressure mapping, opening new possibilities in robotics, medical diagnostics, and smart devices.

Conclusions

In this study, we present a novel approach to fabricate 3D-structured films using localized joule heating, overcoming the limitations of conventional multi-step fabrication methods. The proposed technique enables precise and scalable formation of 3D structures on thermoset elastomers, significantly improving the performance of piezocapacitive soft pressure sensors. Our fabricated sensor demonstrated high sensitivity (1.352 kPa^{-1} in the low-pressure range), fast response time (0.59 s), excellent repeatability, and long-term stability, validating its potential for reliable pressure sensing applications. Furthermore, we have demonstrated the versatility of the developed sensor in various practical scenarios, including subtle pressure detection, fingertip-shaped soft pressure sensor for gripping objects with different weight, and motion monitoring in a shoe insole. Finally, to demonstrate the large-scale and complex pattern fabrication, a multi-pixel pressure array pad was fabricated and evaluated placing different shapes of patterns. As a result, we clearly demonstrated that the suggested 3D-structured films via microheater and localized joule heating could be applied in soft pressure sensors with high performance in terms of sensitivity, scalability, and reliability. We believe that this study paves the way for the advanced fabrication of 3D structures in soft sensors, enabling exceptional sensing performance. Our findings offer a novel approach for developing high-performance pressure sensors with broad applicability in wearable electronics, human-machine interfaces, interactive robotic control, and beyond.

Experimental Section

Fabrication of Localized Joule Heating-induced 3D-structured film

First, a commercial polyimide (PI) film with a thickness of 50 µm (Youngwoo Trading, Korea) was prepared and cleaned the surface with acetone and Isopropyl Alcohol (IPA) to remove any surface contaminants. Laser-induced graphene (LIG) was fabricated by simple and fast CO_2 laser scanning method using a laser cutter (C30, Coryart, Korea) on bare PI film at a scanning power of 30%, speed of 550 mm/s, and spacing of 0.075 mm, respectively. The excess LIG formed on the surface was removed using a N_2 blowing. To apply the uniform voltage at both ends of the LIG, which serve as electrodes, sensing lines were connected to both pads on the electrode pads using a silver nanowire solution (DT-AGNW-N30-IPA, Dittotechnology, Korea) and silver paste (ELCOAT P-10, Jin Chemical, Korea). Then, the film was cured at 60 °C for 30 min to evaporate the solvents. The liquid polydimethylsiloxane (PDMS) precursor (Sylgard 184, Dow Corning Corporation, USA) was prepared by mixing resin and hardener at a 10:1 weight ratio. For uniform mixing and degassing, the PDMS was additionally mixed for 90 s in a 7:6 revolution-rotation ratio using a planetary mixer (KK-V350W, KURABO, Japan). The well-mixed PDMS was poured onto the prefabricated LIG and a thin film applicator was used to control the uniform thickness as 1.5 mm. To apply the heat for localized curing of the PDMS, we set the power supply (Keithley 2100 6.5 Digit USB Multimeter, Tektronix, USA) to control the heating time with a voltage of 30 V. The liquid PDMS precursor was cured by the localized joule heating through the LIG lines. Finally, to remove the remaining liquid PDMS precursor, the film was immersed in silicone cleaner (OS-10 Dow Corning Corporation, USA) for 5 min. The film was then cured at 100°C for 4 h to remove the solvent.

Surface Characterization of the Structured Film

View Article Online
DOI: 10.1039/D5MH00942A

The surface roughness of the fabricated 3D-structured film was measured using a portable surface roughness tester (SJ-120 SURFTESTER, MITUTOYO, Japan) with a scan length of 15 mm. The morphology of the composite film with 3D surface morphology was characterized using a 3D laser scanning confocal microscope (VX-X1050, KEYENCE, Japan). The morphology and composition of the film were characterized by in-situ FE-SEM (JSM7200F, JEOL Ltd., Japan). The process of localized joule heating was measured using a thermal imaging camera (FL
IR A700-STD, FLIR System, USA). A four-point probe (CMT-SR2000N, Advanced Instrument Technology, Korea) was used to measure the sheet resistance of the LIG, and the average and deviation were calculated by measuring 20 points for each condition.

Characterization of the Soft Pressure Sensor

To verify the sensing performance, a high-precision universal testing machine (UTM)(AGS-X (1 kN), Shimadzu Corporation, Japan) equipped with a load cell (maximum load = 1,000 N) was used. A disk with a diameter of 50 mm was used to apply a uniform pressure to the soft pressure sensor. The response of the pressure sensor was measured using LCR (L – inductance, C – capacitance, and R – resistance) meter (3536, Hioki E.E. Corporation, Nagano, Japan) with a bias of 1 V at 200 kHz. The experiment was conducted using a universal tensile compressor at set pressures (1, 3, 5, 7, 9 kPa) and cycles (300 kPa). All the sensor characteristics were evaluated via real-time measurements obtained by connecting the LCR meter to a computer.

Fingertip-based soft pressure sensor application

A fingertip-based soft pressure sensor was fabricated using the following steps [24]. First, Alja Safe powder (SmoothOn, USA) was mixed with water to form a soft elastomer, which was then poured into a beaker. Next, the user's finger was submerged into the mixture for 15 minutes, allowing it to solidify and form a mold tailored for a customized thimble. Once the mold was set, Ecoflex 00-30 (Smooth-On, USA) was evenly distributed within the mold, ensuring full coverage to create the thimble structure. After curing, the soft pressure sensor was placed inside the thimble and encased in a thin layer of Ecoflex 00-30 for additional protection. This experiment was approved by the institutional review board (IRB) of Pukyong National University (PKNU) (2024-08-005).

Author contributions

J. O. performed the sensor testing including sample fabrication and repeat testing, application, etc.; Y. J. and W. L. performed the multi-pixel pressure array patch testing and thermal model simulation of the microheater.; J. O. and J. R. performed the material characterization testing including SEM and EDX.; J. O. and Y. J. wrote the manuscript.; Y. J. and H.C. supervised the research and provided revisions to manuscript. The manuscript was written through contributions of all authors. All authors have given approval to the final version of the manuscript.

Conflicts of interest

There are no conflicts to declare.

Data availability

All data supporting the findings of this study are available within the article and its supplementary information files.

Acknowledgements

This work was supported by the National Research Foundation of Korea (NRF) grant funded by the Korea government (MSIT)(RS-2024-00349451), Pukyong National University Industry-university Cooperation Foundation's 2024(202408190001), Development of green-Hydrogen production system by alkaline-electrolysis/desalination and core parts (KITECH JA-25-0004).

Notes and references

1 X. Wang, L. Dong, H. Zhang, R. Yu, C. Pan and Z. L. Wang, Adv Sci (Weinh), 2015, 2, 1500169.
2 Y. Jung, J. Gu, J. Yeo, W. Lee, H. Han, J. Choi, J. H. Ha, J. Ahn, H. Cho, S. Ryu and I. Park, *Small*, 2024, 20, e2303981.
3 F. Xiao, Z. Wei, Z. Xu, H. Wang, J. Li and J. Zhu, *Adv Sci (Weinh)*, 2025, DOI: 10.1002/advs.202410284, e2410284.
4 J. Seong, J. H. Lee and M. W. Han, *Advanced Materials Technologies*, 2024, DOI: 10.1002/admt.202401306.
5 W. Honda, S. Harada, T. Arie, S. Akita and K. Takei, Advanced Functional Materials, 2014, 24, 3299-3304.
6 K. Kim, J. Choi, Y. Jeong, I. Cho, M. Kim, S. Kim, Y. Oh and I. Park, Adv Healthc Mater, 2019, 8, e1900978.
7 C. Pacini, J. M. Dempster, I. Boyle, E. Goncalves, H. Najgebauer, E. Karakoc, D. van der Meer, A. Barthorpe, H. Lightfoot, P. Jaaks, J. M. McFarland, M. J. Garnett, A. Tsherniak and F. Iorio, Nat Commun, 2021, 12, 1661.
8 J. Tang, K. Gou, C. Wang, M. Wei, Q. Tan and G. Weng, Advanced Functional Materials, 2024, 34
9 Y. Zhang, X. Zhou, N. Zhang, J. Zhu, N. Bai, X. Hou, T. Sun, G. Li, L. Zhao, Y. Chen, L. Wang and C. F. Guo, Nat Commun, 2024, 15, 3048.
10 M. Zhong, L. Zhang, X. Liu, Y. Zhou, M. Zhang, Y. Wang, L. Yang and D. Wei, Chemical Engineering Journal, 2021, 412.
11 C. Xu, J. Chen, Z. Zhu, M. Liu, R. Lan, X. Chen, W. Tang, Y. Zhang and H. Li, Small, 2024, 20, e2306655.
12 J. Park, Y. Lee, J. Hong, M. Ha, Y. D. Jung, H. Lim, S. Y. Kim and H. Ko, ACS Nano, 2014, 8, 4689-4697.
13 Y. Jung, K. K. Jung, D. H. Kim, D. H. Kwak, S. Ahn, J. S. Han and J. S. Ko, Sensors and Actuators A: Physical, 2021, 331.
14 Z. Long, X. Liu, J. Xu, Y. Huang and Z. Wang, Sensors (Basel), 2022, 22.

View Article Online
DOI: 10.1039/D5MH00942A

15 O. Atalay, A. Atalay, J. Gafford and C. Walsh, Advanced Materials Technologies, 2017, 3.
16 B. C. K. Tee, A. Chortos, R. R. Dunn, G. Schwartz, E. Eason and Z. Bao, Advanced Functional Materials, 2014, 24, 5427-5434.
17 Y. Jung, T. Lee, J. Oh, B. G. Park, J. S. Ko, H. Kim, J. P. Yun and H. Cho, ACS Appl Mater Interfaces, 2021, 13, 28975-28984.
18 S. R. A. Ruth and Z. Bao, ACS Appl Mater Interfaces, 2020, 12, 58301-58316.
19 Y. Hu, C. Xu, Y. Zhang, L. Lin, R. L. Snyder and Z. L. Wang, Adv Mater, 2011, 23, 4068-4071.
20 S. Lee, Y. Choi, M. Sung, J. Bae and Y. Choi, Sensors (Basel), 2021, 21
21 F. Bergner, E. Dean-Leon and G. Cheng, Sensors (Basel), 2020, 20.
22 J. Choi, D. Kwon, B. Kim, K. Kang, J. Gu, J. Jo, K. Na, J. Ahn, D. Del Orbe, K. Kim, J. Park, J. Shim, J.-Y. Lee and I. Park, Nano Energy, 2020, 74.
23 Y. Jung, K. K. Jung, D. H. Kim, D. H. Kwak and J. S. Ko, Polymers (Basel), 2020, 12.
24 Y. Jung, J. Choi, W. Lee, J. S. Ko, I. Park and H. Cho, Advanced Functional Materials, 2022, 32.
25 Y. Jeong, J. Gu, J. Byun, J. Ahn, J. Byun, K. Kim, J. Park, J. Ko, J. H. Jeong, M. Amjadi and I. Park, Adv Healthc Mater, 2021, 10, e2001461.
26 Y. Zhang, Y. Hu, P. Zhu, F. Han, Y. Zhu, R. Sun and C. P. Wong, ACS Appl Mater Interfaces, 2017, 9, 35968-35976.
27 S. Baek, H. Jang, S. Y. Kim, H. Jeong, S. Han, Y. Jang, D. H. Kim and H. S. Lee, RSC Advances, 2017, 7, 39420-39426.
28 C. Xu, Y. Wang, J. Zhang, J. Wan, Z. Xiang, Z. Nie, J. Xu, X. Lin, P. Zhao and Y. Wang, Science Advances, 2024, 10, eadp6094.
29 H. Moeinnia, D. J. Agron, C. Ganzert, L. Schubert and W. S. Kim, npj Flexible Electronics, 2024, 8.
30 J. Lee and H. So, Microsyst Nanoeng, 2023, 9, 44.
31 Y. Mao, B. Ji, G. Chen, C. Hao, B. Zhou and Y. Tian, ACS Applied Nano Materials, 2019, 2, 3196-3205.
32 T. Ageyeva, S. Horvath and J. G. Kovacs, Sensors (Basel), 2019, 19.
33 J. Lin, Z. Peng, Y. Liu, F. Ruiz-Zepeda, R. Ye, E. L. Samuel, M. J. Yacaman, B. I. Yakobson and J. M. Tour, Nat Commun, 2014, 5, 5714.
34 T. Yang, W. Deng, X. Chu, X. Wang, Y. Hu, X. Fan, et al. ACS nano 2021,15.
35 S. Chen, S. Peng, W. Sun, G. Gu, Q. Zhang and X. Guo, Advanced Materials Technologies, 2019, 4.
36 J. Shi, L. Wang, Z. Dai, L. Zhao, M. Du, H. Li and Y. Fang, Small, 2018, 14, 1800819.
37 H. Kim, G. Kim, T. Kim, S. Lee, D. Kang, M. S. Hwang, Y. Chae, S. Kang, H. Lee and H. G. Park, Small, 2018, 14, 1703432.
38 S. Wan, H. Bi, Y. Zhou, X. Xie, S. Su, K. Yin and L. Sun, Carbon, 2017, 114, 209-216.
39 X. Shuai, P. Zhu, W. Zeng, Y. Hu, X. Liang, Y. Zhang, R. Sun and C.-p. Wong, ACS applied materials & interfaces, 2017, 9.